

**Drastic slowdown of the Rayleigh-like wave in unjammed granular suspensions**

Javier Brum,<sup>\*</sup> Jean Luc Gennisson,<sup>†</sup> Mathias Fink, Arnaud Tourin, and Xiaoping Jia<sup>‡</sup>  
*Institut Langevin, ESPCI Paris, PSL University, CNRS, 1 rue Jussieu, 75005 Paris, France*



(Received 14 November 2018; published 15 April 2019)

We present an experimental investigation of Rayleigh-like wave propagation along the surface of a dense granular suspension. Using an ultrafast ultrasound scanner, we monitor the softening of the shear modulus via the Rayleigh-like wave velocity slowdown in the optically opaque medium as the driving amplitude increases. For such nonlinear behavior two regimes are found when increasing the driving amplitude progressively: First, we observe a significant shear modulus weakening due to the microslip on the contact level without macroscopic rearrangements of grains. Second, there is a clear macroscopic plastic rearrangement accompanied by a modulus decrease up to 88%. A friction model is proposed to describe the interplay between nonlinear elasticity and plasticity, which highlights the crucial effect of contact slipping before contact breaking or loss. Investigation of this nonlinear Rayleigh-like wave may bridge the gap between two disjoint approaches for describing the dynamics near unjamming: linear elastic soft modes and nonlinear collisional shock.

DOI: [10.1103/PhysRevE.99.042902](https://doi.org/10.1103/PhysRevE.99.042902)

**I. INTRODUCTION**

The jamming transition is a general paradigm for understanding how complex fluids such as foams, emulsions, and granular materials develop rigidity: when the density of randomly packed particles is increased to a certain critical value, the viscosity increases dramatically and the flow is arrested [1–6]. Reciprocally, amorphous solids made of athermal particles like bubbles, droplets, and grains lose shear rigidity and make a transition to a liquid state when the confining pressure vanishes [7]. Numerical simulations of frictionless particles show that an effective medium description fails near unjamming due to nonaffine motion of particles and that the critical scaling of the shear modulus is correlated to soft modes [8–10]. Understanding the mechanical response across this solidlike-to-liquidlike transition remains a major challenge for real granular matter because of the friction and the strong nonlinearity at vanishing confining pressure [11–13] where the particle packing does not tend to isostaticity [4,10]. Addressing this issue is also of great importance for industrial applications and geophysical processes such as landslides [14].

In both dry and water-saturated granular materials, force transmission and elastic wave propagation strongly depend on the inhomogeneous and metastable contact force network [2,5,8]. As the confining pressure  $P$  decreases, the effective medium theory [8], based on the affine approximation and the Hertz-Mindlin contact law, predicts that in the linear

regime both the bulk  $K$  and the shear  $G$  modulus scale as  $\sim P^{1/3}$ . However, numerical simulations in frictionless sphere packings reveal that  $G$  vanishes with pressure as  $\sim P^{2/3}$  due to the nonaffine deformation [4,7–9]. Nonlinear responses beyond linear elasticity have also been investigated by using finite shear strain to study the transition from a jammed to a flowing state [15–17].

Sound propagation in granular media provides a very efficient and controlled way to perform dynamic measurements that can be compared naturally with theory and simulations based on elasticity. The long-wavelength coherent wave gives access to the effective modulus, whereas the short-wavelength scattered waves are sensitive to any rearrangement of the contact force network [18]. In the linear regime, velocity measurements of coherent sound waves allow monitoring of the weakening of jammed media when the confining pressure is decreased [8,19,20] or when a static shear is applied [20,21]. High-amplitude ultrasound can act as a pump to soften the jammed solid in a nonlinear regime as shown by using compressional waves [22–24]. Another dynamic approach using shock waves has also been proposed to investigate the unjamming transition in granular media [25,26]. In this highly nonlinear regime, the dynamic displacement is larger than the grain overlap induced by the confining pressure so that elastic wave propagation becomes impossible, i.e., in sonic vacuum [27]. Instead, solitonlike shocks travel via collisions at a front speed depending on the particle velocity. Recently, it has been reported that such shocks or impacts may induce dynamic shear jamming in granular suspensions [28] or may propagate in dense colloidal suspensions [29] in the presence of saturating liquid.

In this work, we investigate the unjamming transition by new measurements of high-amplitude *Rayleigh-like waves* in a weakly jammed granular suspension. Unlike oscillatory rheological measurements [17], these acoustic measurements allow us to monitor *locally* the shear modulus softening as

<sup>\*</sup>Current address: Instituto de Física, Facultad de Ciencias, Universidad de la República, Montevideo, Uruguay.

<sup>†</sup>Current address: IR4M, CNRS, Université Paris Sud, CEA Service Hospitalier F. Joliot, Orsay, France.

<sup>‡</sup>Corresponding author: [xiaoping.jia@espci.fr](mailto:xiaoping.jia@espci.fr); also at Université Paris-Est Marne-la-Vallée, France.

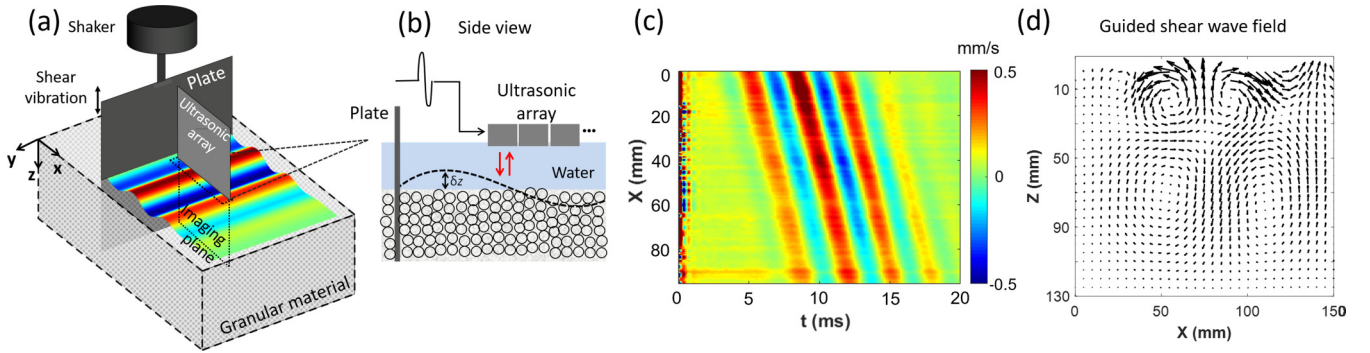


FIG. 1. Experimental investigation of the Rayleigh-like wave along the surface of a granular medium. (a) Sketch of the experimental setup: the wave is excited by a rough plate in a water-saturated glass-bead packing. (b) The out-of-plane particle displacement ( $\delta z$ ) and velocity at the sample surface are inferred from the cross correlation of successive backscattered ultrasonic speckles acquired with an ultrafast ultrasonic scanner. (c) Typical seismogram measured after the generation of a shear pulse centered at 300 Hz; the particle velocity is plotted versus the time  $t$  and distance  $x$  from the source (see Appendix A for details). (d) Snapshot of the vector displacement field of the Rayleigh-like surface mode calculated with free surface and clamped bottom boundary conditions in an inhomogeneous layer (see Appendix B for details).

the driving amplitude increases, along the wave path and inside optically opaque dense granular suspensions, till the onset of the plastic rearrangement of grains. We analyze these nonlinear elastic responses using mean-field descriptions for frictional sphere packings. Elastic waves are used here both as a pump to fluidize the granular solid and as a probe of the material softening.

## II. EXPERIMENT

Weakly jammed granular media under investigation are made with glass beads of diameter  $d \approx 250 \mu\text{m}$ , confined in a rectangular box with a free surface [Fig. 1(a)]. The glass beads settle down in water under gravity, which creates a dense granular suspension ( $h \approx 13 \text{ cm}$  in height) with a packing density  $\phi \simeq 0.6$ . A rough metallic plate (with a surface of  $\Sigma_o \approx 10 \times 10 \text{ cm}^2$ ) glued with sand particles acts as a shear excitation source. It is excited by a shaker with a four-cycle tone burst centered at a frequency between 100 and 500 Hz. The static load applied to the plate,  $W = P\Sigma_o \approx 6.5 \text{ N}$ , can be estimated from the mean confining pressure  $P \simeq [\phi(\rho_g - \rho_w) + (1 - \phi)\rho_w]gL/2 \approx 650 \text{ Pa}$ , with  $\rho_g = 2500 \text{ kg/m}^3$  and  $\rho_w = 1000 \text{ kg/m}^3$  the density of glass and water, respectively, and  $L \approx 10 \text{ cm}$ . Oscillating shear force  $F_{ac}$  and acceleration  $a_{ac}$  are measured by a force sensor and an accelerometer, respectively.

As shown in Fig. 1(d), the source excites a Rayleigh-like surface wave [11,30] with a group velocity close to the shear wave velocity  $V_S$  (see Appendix B for details). To investigate the propagation of this low-frequency surface guided mode we used an ultrafast ultrasound scanner (Aixplorer) that was originally developed in our laboratory to track tissue motion induced by low-speed shear waves in the context of medical imaging [31]. The same kind of scanner, which can acquire images up to 200 times faster than conventional ultrasound systems, was also used for rheology measurements in complex fluids [32].

Figure 1(b) depicts a 192-element ultrasonic array (centred at 4 MHz) placed in water close to the surface of the granular suspension and parallel to the propagation direction ( $x$  axis). After the generation of the guided wave, the ultrafast

ultrasonic scanner acquires successive backscattered ultrasonic speckle patterns from the granular sample at a frame rate of  $f_{RF} = 16 \text{ kHz}$ . The arrival time of a given speckle pattern corresponds to a specific location of grains within the medium. By cross-correlating in time the speckle observed from one frame to the next (i.e., speckle interferometry [32]), a speckle-tracking algorithm estimates the particle velocities along the ultrasonic beam direction  $v_z = \delta z / \delta t$  with  $\delta t = 1/f_{RF}$  [see Fig. 1(b) and Appendix A]. Figure 1(c) shows a typical resulting seismogram at the surface of the bead packing ( $z = 0$ ) after a source excitation at a central frequency of  $f = 300 \text{ Hz}$  and with a low amplitude,  $F_{ac} \sim 0.19 \text{ N}$ . The measured particle velocity along the  $z$  axis is of the order of  $v_{ac} \sim 0.4 \text{ mm/s}$ , which corresponds to a particle displacement  $u_{ac} (=v_{ac}/(2\pi f)) \sim 0.3 \mu\text{m}$ , i.e., much less than the particle diameter. The group velocity of the short pulse is measured via cross-correlation of the wave train, being  $V_G \sim 25 \text{ m/s}$ . This gives a dynamic strain  $\gamma_{ac} (= \partial u / \partial x = (2\pi f / V)u_{ac}) \sim 2 \times 10^{-5}$ , with  $V \sim V_G$  the phase velocity.

The main goal of this work was to monitor the shear modulus softening near unjamming in a realistic granular medium (i.e., frictional and optically opaque). When the driving amplitude is increased, a significant increase in the Rayleigh-like wave pulse time of flight is clearly observed [Fig. 2(a)], corresponding to a slowdown of the group wave velocity  $V_G$  up to 30%–50% as shown in Fig. 2(b). Such a velocity decrease is about 3 times larger than that observed with compressional waves [23,24]. We also detect the generation of second and third harmonics whose amplitudes evolve as a function of the propagation distance [Fig. 2(c)]. This observation is different from those with shear shock waves propagating in homogeneous soft solids (like gels), where only odd harmonics are observed but without any significant change in the wave velocity ( $<1\%$ ) [31].

Note that despite the important slowdown of the wave velocity  $\Delta V_G / V_G$  [Fig. 2(b)], presumably due to the modification of the contact network [23], we do not observe any visible rearrangement of grain positions. A similar behavior was observed in another kind of dynamic experiment where a dense granular suspension was subject to a sinusoidal oscillation with comparable shaking amplitude and frequency [33]. The

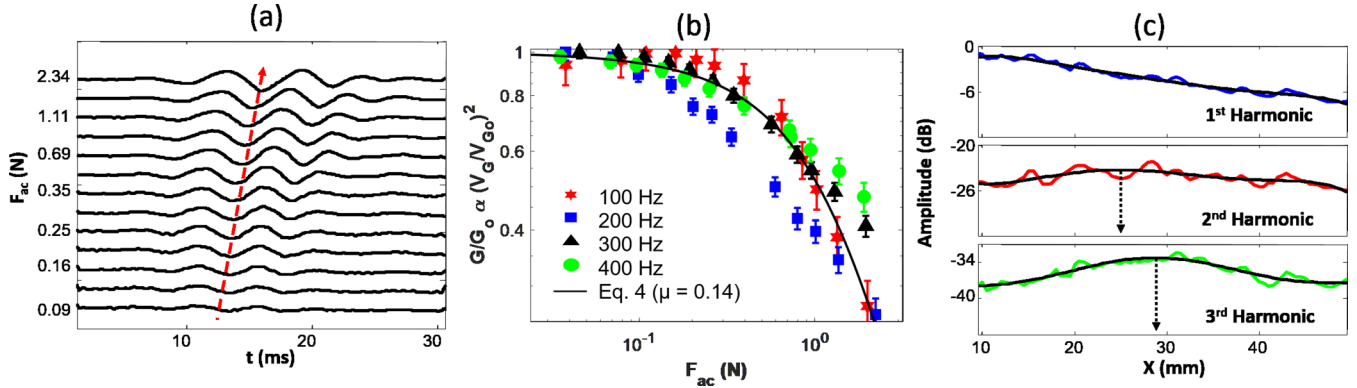


FIG. 2. Nonlinear acoustic responses of a Rayleigh-like wave in a fragile granular packing. (a) Wave pulse recorded at  $x = 95.5$  mm from the source; the travel time of the surface wave increases with the shear driving force  $F_{ac}$ . (b) Softening of the shear modulus  $G$  (or group velocity  $V_G$  slowdown) as a function of the driving force  $F_{ac}$  in a case where no visible rearrangements of grains is observed. The solid line is the prediction by the friction model. (c) Amplitudes of the fundamental (100-Hz) and of the second and third harmonics versus the propagation distance after an excitation at  $F_{ac} \approx 2$  N. The maximum is indicated by an arrow after smoothing (solid lines).

absence of plastic rearrangement of grains can be explained as follows: on the one hand, the typical acoustic displacement is relatively small compared to one grain diameter, i.e.,  $u_{ac} < 5 \mu\text{m} \sim d/50$ ). On the other hand, the characteristic time for rearrangement (measured by the time it takes for a grain to move from one cage to the next one over a distance  $\sim d$ ) is large compared to the period of driving. More precisely, we find that the fall time for the granular suspension is [34]  $t_{fall} [= \eta_f / (P_g \alpha)] \sim 20$  ms with the viscosity of water  $\eta_f \sim 10^{-3}$  Pa  $\cdot$  s, permeability parameter  $\alpha \sim 0.01$ , and confining pressure  $P_g \sim \phi(\rho_g - \rho_w)gd \sim 2.25$  Pa (the layer at the top surface is the most likely to be subjected to possible grain motion [35]). For the vibration frequency range explored in our experiments ( $f = 100$ – $500$  Hz), the period of oscillatory driving is  $T_o = 1/f \sim 4$  ms, which leads to  $T_o$  smaller than  $t_{fall}$  (in water-saturated glass-bead packings). Under such conditions, we expect that the grains in the granular suspension do not have the time to move or rearrange to the new cages before the applied vibration changes the driving direction.

Nevertheless, by further increasing the driving amplitude, plastic deformation of the granular packing should become possible. To detect it, we examine the change in ultrasonic speckle patterns, i.e., B-mode images [31] (see Appendix A) recorded before, during, and after the passage of the nonlinear Rayleigh-like wave [Figs. 3(a) and 3(b)]. As the characteristic length for rearrangement corresponds to the grain size  $d$  [Fig. 3(c)], it falls in the spatial resolution of the ultrasound used here  $\lambda_{US}/2 \sim 180 \mu\text{m}$  ( $\lambda_{US}$  is the wavelength in water). Figure 3(b) (right panel) shows the case of a change in the speckle pattern for the large shear driving  $F_{ac} \approx 2.7$  N ( $\gamma_{ac} \sim 4 \times 10^{-3}$ ) at the lower frequency of 100 Hz. Here the measured particle velocity reaches the very high value of  $v_{ac} \sim 25$  mm/s and the particle displacement, more than  $u_{ac} \sim 40 \mu\text{m}$ , becomes important compared to the grain size  $d \sim 250 \mu\text{m}$ . This observation confirms the occurrence of an unjamming accompanied by a rearrangement of grain positions. The plastically fluidized zone appears close to the driving source within  $x \sim 30$  mm and along a depth  $z \sim 7$  mm as shown in the right panel in Fig. 3(b). In the seismogram detected at the surface of the bead packing [Fig. 3(c)], two slopes

are observed to be associated, respectively, with the fluidized zone and the unjammed zone without plastic rearrangement of grains. The wave velocity in the fluidized zone ( $x < 30$  mm) is reduced to 6 m/s!

### III. DISCUSSION AND MODELING

#### A. Linear elasticity

We use the mean-field approach as a guide to interpret our experimental data. According to the Biot/Gassmann theory for a fluid-saturated granular porous medium [36], the saturating liquid increases the bulk modulus of the medium and couple compressional waves in the solid and liquid phases to form a fast ( $V_P$ ) and a slow ( $V_{P2}$ ) mode but does not affect the shear modulus (water responds little to shear forces) provided that the elastic moduli of the solid skeleton ( $K$  and  $G$ ) remain unchanged. It only influences the shear wave velocity through inertial effects,  $V_S = (G/\rho)^{1/2}$ , where the average density is  $\rho \simeq [\phi\rho_g + (1 - \phi)\rho_w]$ . Bourbié *et al.* (and Deresiewicz) have also examined what happens to the Rayleigh wave at the free surface of a saturated porous medium described by the Biot theory [37]. It was shown that for the low-frequency range (as considered here), one recovers the classic equation of the Rayleigh wave velocity  $V_R$  (depending on  $V_P$  and  $V_S$ ), whose property is mainly determined by the shear modulus  $G$  (or  $V_S$ ). Nevertheless, for a granular packing, the elasticity arises from the externally applied confining stress that forms the contact network, i.e., the solid skeleton. The presence of saturating liquid (water) may thus affect the shear modulus of the granular skeleton, either by decreasing the effective confining pressure via the pore pressure or by modifying the contacts (network) between grains via lubricated friction and/or viscous slipping [38].

To understand qualitatively the slowdown of the Rayleigh-like wave in dense granular suspensions when the driving amplitude is increased, we primarily focus on the shear modulus of the solid skeleton modeled by the effective medium theory [8,19] for (dry) random packing of frictional spheres. Based on the affine approximation, the effective medium theory has provided an adequate description of low-amplitude ultrasonic

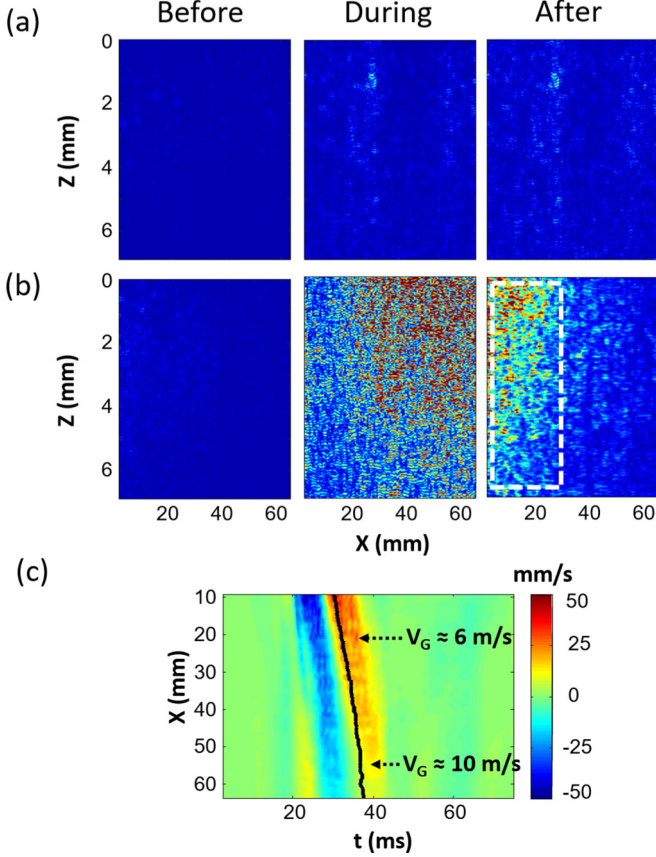


FIG. 3. Ultrasound imaging of grain motion during plastic granular rearrangement. Comparison of the ultrasonic speckle patterns recorded before, during, and after the Rayleigh-like wave passage after an excitation at 100 Hz by (a) a small force,  $F_{ac} \sim 0.03$  N, and (b) a large one,  $F_{ac} \sim 2.7$  N. The latter induces the rearrangement of grains localized in a zone close to the driving (right panel; white rectangle). (c) Scenario of the unjamming accompanied by grain motion via the dilatancy. The seismogram in the plastically deformed zone reveals a group velocity of  $V_G \sim 6$  m/s.

experiments in highly compressed granular solids [23], in situations where configuration-specific multiply scattered elastic waves do not probe any significant rearrangement of the contact force network. Such reversible sound-matter interaction [18,23] is also consistent with previous works where the linear elastic response was observed at frictional interfaces due to pinned asperities [39]. For isotropic confining pressure  $P$  (or load  $W$ ), the bulk and shear moduli of the granular packing (i.e., solid skeleton) can then be related to the normal and tangential contact stiffness  $k_n$  and  $k_t$  as [40]  $K \sim \phi Z k_n$  and  $G \sim \phi Z (k_n + 3k_t/2)$ , with  $Z$  the average coordination number and  $\phi$  the packing density of spheres [Fig. 4(a)]. For the Hertz-Mindlin contact [8,40] the contact stiffnesses  $k_n$  and  $k_t$  ( $\sim k_n$ ) at low oscillation amplitudes are related to the contact area (of diameter  $a$ ) and thus to the static compression or overlap  $u_o$  ( $\sim a^2/2R$ ) under a normal load  $w$ ,  $k_n \sim a \sim w^{1/3}$  [Fig. 4(b)]; accordingly, on the macroscopic scale,  $K$  and  $G$  scale with pressure as  $\sim P^{1/3}$ .

However, for oscillatory shear (acoustic) measurements in weakly confined granular packings considered here, the

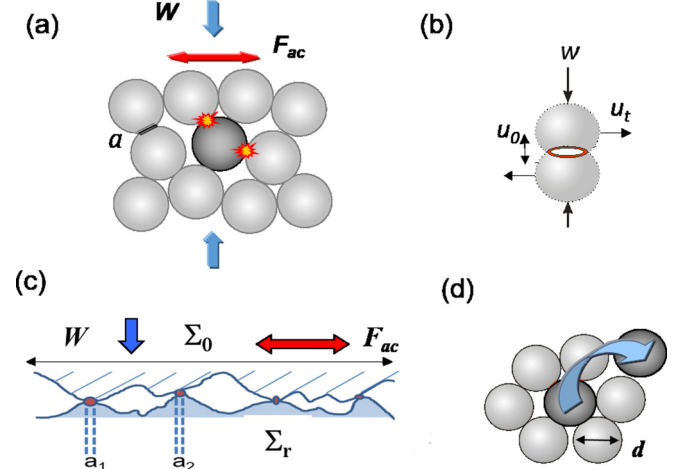


FIG. 4. (a) Confined elastic sphere packing (contact network) under shear. (b) Hertz-Mindlin contact model. (c) Multicontacts (asperities) formed between rough solid surfaces. (d) Scenario of the unjamming accompanied by grain rearrangement.

affine approximation may break down even at a relatively low amplitude of vibration due to induced slipping between grains and/or rearrangement of grain positions [7,8]. Consequently, the shear modulus can be overestimated by the effective medium theory, which does not allow the grains to relax via nonaffine motion [4,8]. Numerical simulations show that the scaling of the linear shear modulus versus the confining pressure shall be rewritten for both frictionless and frictional packings as [3,4,9],

$$G \sim K \Delta Z \sim k Z \Delta Z, \quad (1)$$

where  $k$  is a linear combination of  $k_n$  and  $k_t$  and  $\Delta Z = Z - Z_{iso}$  is the excess contact number (measuring the distance to isotaticity), which is related to the excess packing density by  $\Delta\phi \sim (\Delta Z)^2$  with  $\Delta\phi = \phi - \phi_{iso}$  [3,9]. Note that the nonaffine relaxation barely modifies the bulk modulus, i.e., the scaling remains  $K \sim P^{1/3}$  for the Hertz-Mindlin interaction. For a three-dimensional (3D) packing of frictionless spheres ( $Z_{iso} = 6$  and  $\phi_{iso} = 0.64$ ), as grain overlap (compression)  $u_o$  and consequently  $\Delta\phi$  scale as  $\sim P^{2/3}$ , one has  $\Delta Z \sim P^{1/3}$ , hence leading to  $G \sim P^{2/3}$  and  $V_S \sim P^{1/3}$ . For frictional spheres, the packing does not tend to the isotatic value ( $Z_{iso} = 4$ ) at unjamming under vanishing  $P = 0$ , but to a critical contact number,  $Z_c > Z_{iso}$  [3,10]. The precise value of  $Z_c$  depends on the friction between grains and the preparation history. The fact that  $Z_c$  remains larger than  $Z_{iso}$  explains why the shear modulus  $G$  does not vanish at  $P = 0$  [Eq. (1)] and why it is possible to have a linear response of guided surface waves propagating along the free surface at small dynamic strain  $\gamma_{ac} < 10^{-5}$  in our granular suspensions [Fig. 2(b)] and also in dry granular packings [11]. Furthermore, even in the absence of an external load, compacted granular materials always have internal stresses which build up from friction between the grains (i.e., interlock) and from constraints imposed by the material boundary [20,41].

### B. Nonlinear elasticity in frictionless packings

We now discuss the nonlinear response of granular packings under finite shear beyond linear elasticity, either by steady [16] and oscillatory shear [15,17] or by nonlinear acoustics in this study. Our measurements show that the shear modulus softening in our frictional granular packing exhibits three regimes, depending on the dynamic strain  $\gamma_{ac}$ . In regime (i), at low amplitudes  $\gamma_{ac} (\leq 10^{-5})$ , the wave velocity is constant; regime (ii) corresponds to higher driving amplitudes where the velocity decreases continuously without visible grain rearrangement [Fig. 2(b)], down to the final regime, (iii), accompanied by the plastic rearrangement of grains [Fig. 3(c)]. To analyze these data, we first consider the extension of the shear modulus scaling law [Eq. (1)] beyond linear elasticity postulated by Otsuki and Hayakawa for a *frictionless* soft sphere packing,  $G(\Delta Z, \gamma_o) \sim K \Delta Z g[\gamma_o/(\Delta Z)^2]$  (we express  $G$  as a function of  $\Delta Z$  instead of  $\Delta\phi$ ), as in [15]. Here  $g(x)$  is a scaling function with the asymptotic behavior  $g(x) \rightarrow \text{constant}$  when  $x \rightarrow 0$  and  $g(x) \rightarrow x^{-1/2}$  when  $x \rightarrow \infty$ . The former recovers the linear response [Eq. (1)], whereas the latter allows accounting for the shear modulus softening at large shear  $\gamma_o$ ,

$$G(\Delta Z, \gamma_o) \sim K(\Delta Z)^2 \gamma_o^{-1/2}. \quad (2)$$

This scaling of  $G$  with the amplitude  $\gamma_o$  of the oscillatory shear can be explained based on an elastoplastic model, which consists of an infinite number of connections in series with an elastic element of equal shear modulus  $G_o$  and a slip element characterized by the drop stress  $s$  (avalanche process). The stress of an individual element  $\tilde{S}(s, t) = G_o \gamma(t)$  is a linear function of the imposed strain  $\gamma(t) = \gamma_o(1 \cos(\omega t))$ , but it drops to 0 when exceeding the maximum value  $s$  due to the breaking of the contact or bond [Fig. 4(a)]. The shear modulus of the individual element is then calculated by  $\tilde{G}(\gamma_o, s) = (-\omega/\pi) \int_0^{2\pi/\omega} \tilde{S}(s, t) \cos(\omega t) dt / \gamma$  and the global shear modulus is given by  $G(\gamma_o) = \int_0^\infty ds \tilde{G}(\gamma_o, s) \rho(s)$ . Here  $\rho(s) \sim s^{-3/2} \exp(-s/s_c)$  is the probability density of the stress drop (with  $s_c$  a characteristic stress), larger than the lower cutoff stress drop  $s_o$  caused by the rearrangement of one grain. For  $s_o/G_o \ll \gamma_o \ll s_c/G_o$ , the shear modulus scales finally with  $\gamma_o$  as  $G \sim G_o^{1/2} \gamma_o^{-1/2}$  and is independent of  $\omega$ . On the other hand, Eq. (2) reveals a power law for the scaling of the excess contact number  $\Delta Z$  (or packing density  $\Delta\phi$ ) different from that of Eq. (1), which probably pertains to the rearrangement of grains via shear dilatancy caused by large shear [16]. However, the shear modulus softening observed in our experiments [Fig. 2(b)] is not necessarily associated with such plastic rearrangement.

### C. Nonlinear elasticity in frictional packings

To specify the nonlinear elasticity of  $G(\gamma_o)$  in realistic granular media, we propose a heuristic model where we replace the above elastoplastic element with the Hertz-Mindlin frictional contact [Fig. 4(b)]. This contact is relevant not only between grains in granular media [Fig. 4(a)] but also in tribology and solid friction between asperities [Fig. 4(c)]. Two distinct kinds of nonlinearity come into play at the contact area between two elastic spheres at high-amplitude vibration.

In the normal direction, the Hertz contact law provides a relation between the oscillating force  $f_n$  and the displacement  $u_n$ ,  $f_n \approx k_n u_n (1 + \beta u_n + \delta u_n^2)$  when  $u_n \ll u_o$  (with the contact kept compressed).  $\beta = 1/(4u_o)$  and  $\delta = 1/(24u_o^2)$  are the quadratic and cubic nonlinear terms determined by  $u_o \sim w^{2/3}$ . It is presumably responsible for the harmonics generation [23] [Fig. 2(c)] but hardly affects the normal stiffness  $k_n^{\text{NL}} (= f_n/u_n) \approx k_n(1 + \delta u_n^2)$ , which corresponds to an average value over one cycle of oscillation. The other nonlinearity stems from the tangential friction, where the Mindlin theory predicts both a nonlinear elasticity and dissipation from the hysteresis loop of force displacement [23,42]. This hysteretic nonlinearity causes a weakening in the tangential stiffness  $k_t^{\text{NL}} (= f_t/u_t) \sim k_t(1 - f_t^*/6\mu w)$ , proportional to the amplitude of the tangential oscillating force  $f_t^*$  to lowest order ( $\mu$  is the interparticle friction coefficient). Therefore, for moderate vibration  $u_n < u_o$  and  $f_t^* < \mu w$ , the shear stiffness softening is dominant compared to the normal stiffness softening [22]; it predicts a shear velocity decrease for a moderately high shear  $f_t^* < \mu w$  before reaching the yield of sliding,

$$\Delta V_S/V_S \sim (1/2)\Delta k_t/k_t \sim f_t^*/(6\mu w), \quad (3)$$

which is about 10% for  $f_t^*/w \sim F_{ac}/W \sim 0.15$  (with  $F_{ac} \sim 0.8$  N and  $W \sim 6.5$  N) and  $\mu \sim 0.2$ . Unlike the mechanism of softening invoked in Eq. (2), the present slip-induced softening can occur with the grains kept in contact during oscillation ( $a > 0$  and  $u_o > 0$ ). This scenario may partly explain our observation of the dynamic modulus softening up to  $\Delta V_S/V_S \sim 40\%$  [Fig. 2(b)] without macroscopic rearrangement of particles. Similarly, such slipping-induced softening of the shear interfacial stiffness was also found between one grain (granular layer) and a substrate by the shear ultrasonic oscillation under a low confining pressure, i.e., gravity. The necessary vibrational energy for rearranging the grains by sliding is about 2 orders of magnitude smaller than the energy barrier by jumping a surface asperity [42].

In a weakly granular packing compressed by gravity, the contact network is very inhomogeneous and the distribution of the (normal) contact force  $w$  is exponential [8],  $\rho(w) \sim \exp(-w/w_c)$ , with  $w_c$  a characteristic force. This would give rise to the same distribution for the yield force  $f_s = \mu w$  at the grain contacts, similar to the above drop stress distribution for the slip elements [Eq. (2)]. Under finite oscillatory shear, the hertzian contacts (or bonds) of smaller diameters  $a \sim w^{1/3}$  will first break down via slipping, which leads to the softening of interfacial shear stiffness but keeps the contacts overlapped. On the macroscopic level, the shear modulus softening or the unjamming sets on without rearrangement of the grain positions, and consequently both the coordination number  $Z$  and the packing density  $\phi$  remain almost unchanged [Figs. 2(b) and 4(a)]. Apparently, this softening process in a 3D sphere packing is comparable to what happens on a multicontact interface under oscillatory shear [39] [Fig. 4(c)], where the distribution  $\rho(\delta)$  of the overlap  $\delta$  or compression  $u_o$  (or diameter  $a$ ) between two asperities is also exponential.

To further investigate this similarity, we follow Bureau *et al.* [39] to extend the Mindlin model for a single contact to the case of multiple microcontacts in which we replace the asperities formed between 2D rough surfaces

[Fig. 4(c)] by the bead contacts in 3D granular packings [Fig. 4(a)]. When the interface or the granular medium is loaded, the macroscopic shear force  $F(t)$ , or stress  $\tau(t)$ , is the sum of the contribution from all contacts  $\rho(\delta)$ . With a macroscopic shear force (or stress) of the form  $F(t) = F_{dc} + F_{ac} \cos(\omega t)$ , the shear displacement  $U_i(t)$  [or strain  $\gamma(t)$ ] is analytically derived using the distribution  $\rho(\delta)$  over one cycle and the elastic response  $U_{ac}$  (or  $\gamma_{ac}$ ) is then obtained by  $U_{ac} = (\omega/\pi) \int_0^{2\pi/\omega} U_i(t) \cos(\omega t) dt \approx 2\mu\lambda[(F_{ac}/2\mu W) + (F_{ac}/2\mu W)^2 + (5/4)(F_{ac}/2\mu W)^3]$ , with  $\lambda$  a characteristic elastic length. The softening of the apparent shear stiffness by  $k_t = F_{ac}/U_{ac}$  or shear modulus  $G = \tau_{ac}/\gamma_{ac}$  may thus be written as a function of the dynamic amplitude,

$$G/G_o \sim k/k_{t,o} = 1/[1 + F_{ac}/2\mu W + (5/4)(F_{ac}/2\mu W)^2], \quad (4)$$

where  $G_o$  ( $k_{t,o}$ ) is the linear shear modulus (stiffness) at small  $F_{ac}$ . As expected for solid friction, the deduced shear modulus and stiffness are independent of  $\omega$ . The prediction from Eq. (4) shows a reasonably good agreement with the measured data, highlighting the crucial role of contact slipping in the shear modulus softening and the onset of unjamming [23,39,42]. The fitted friction coefficient  $\mu \sim 0.14$  is a bit low but comparable to other (dry) measurements ( $\mu \sim 0.25$ ) [42], suggesting a possible liquid-induced lubrication effect.

#### D. Plastic rearrangement

Let us finally examine the shear modulus softening in the unjammed state accompanied by the rearrangement of the grain positions [Fig. 3(b)] produced at the strongest shear driving  $\gamma_{ac} \sim 4 \times 10^{-3}$ . This nonlinear response is obviously associated with the change in the packing density  $\Delta\phi$  and, accordingly, in the coordination number  $\Delta Z \sim (\Delta\phi)^{1/2}$ . Figure 3(c) shows that the wave velocity decreases from an averaged value of 17 m/s at 100 Hz to a smallest value of 6 m/s in the fluidized zone close to the shear driving ( $<20$  mm). Such a huge velocity slowdown,  $\Delta V_G/V_G \sim \Delta V_S/V_S \sim 65\%$ , corresponds to a shear modulus weakening ( $G = \rho V_S^2$ ) of  $\Delta G/G \sim 88\%$ ! We believe that the grain rearrangement via shear dilatancy [Fig. 4(d)] should also exist in the moderate nonlinear regime [Fig. 2(b)] where the rearrangement of grains may be too small ( $<d/5 \sim \lambda_{US}/10$ ) to be detected due to the resolution of ultrasound imaging (with possible contact breaking). These experiments evidence that the nonlinear shear response at finite acoustic strain is substantially plastic in the vicinity of unjamming transition where nonlinear elasticity cannot be decoupled from plasticity, a picture proposed by the simulation for athermal amorphous solids [43]. Further investigation of the shear modulus softening or unjamming is needed to quantify the interplay between vibration-induced contact slipping [Eq. (4)] and contact breaking (loss)  $\Delta Z < 0$  observed in discrete-element-method simulations [44] (occurring, however, with a dynamic strain about 2 orders of magnitude larger due to the absence of the nonlinear tangential Mindlin contact) or shear dilatancy  $\Delta\phi < 0$  accompanied by grain rearrangement [Eq. (2)] and merge these two mechanisms into a unique model.

#### IV. CONCLUSION

In summary, we have investigated a Rayleigh-like wave propagation in weakly jammed dense granular suspensions. We monitored the unjamming transition by measuring the softening of the shear modulus with increasing amplitude of the oscillatory shear via the surface wave velocity slowdown. Regarding the unjamming transition, two successive processes were found when the driving was progressively increased: contact slipping without any change in the packing density (and of the contact number) on the micro- or nanometric scale and plastic rearrangement of grains via shear dilatancy on the macroscopic scale. Our measurements are consistent with the nonaffine models in frictionless packings and agree particularly well with the extension of the Mindlin friction model on nonlinear elasticity, which evidences the important effects of contact slipping without contact loss. This scenario of unjamming by acoustic fluidization/lubrication [23,42,45] should be helpful to better understand how transient seismic waves trigger avalanches and earthquakes [22] in sheared granular media.

#### ACKNOWLEDGMENTS

We thank C. Caroli and M. Tanter for helpful discussions. J.B. acknowledges the support from Instituto de Física, Facultad de Ciencias, Universidad de la República, Montevideo, Uruguay, and ANII, Uruguay. This work was supported by French LABEX WIFI under references ANR-10-LABX-24 and ANR-10-IDEX-0001-02 PSL.

#### APPENDIX A: ULTRAFAST ULTRASOUND IMAGING

To investigate low-frequency Rayleigh-like wave propagation and its effects on granular packing, ultrafast ultrasound imaging was used. Through ultrasound it is possible (i) to image a cross-sectional plane of the granular packing (as usually done in ultrasonography) and (ii) to measure the axial particle velocity field associated with wave propagation within the sample. To this end, the sample is insonified with ultrasonic waves emitted from an ultrasonic array. Each of the 192 elements in the array emits simultaneously a two-cycle short pulse centered at 4 MHz, thus generating a pulsed plane wave that propagates in the  $xz$  plane in a direction perpendicular to the surface of the sample [Fig. 5(a)]. This plane wave is scattered off the beads and the corresponding backscattered echoes are recorded by each element of the transducer array [Fig. 5(b)]. The backscattered signal comes from the superposition of the echoes coming from different scatterers within the medium. Therefore, a beam-forming step is necessary to construct an ultrasonic image, i.e., to relate the arrival time of an ultrasound echo to a given position within the imaging plane. In this work a standard parallel beam-forming algorithm was used. Each point  $(x, z)$  in the image is obtained by adding coherently all the contributions coming from it. Toward that goal a time delay of the form  $T(x, z) = \sqrt{(z^2 + (x - x_i)^2)}/c$  is first applied to the backscattered signals, where  $x_i$  corresponds to the position of the  $i$ th element in the ultrasonic array and  $c$  is the speed of sound ( $=1500$  m/s in water) [Fig. 5(c)]. Then the 192 time-delayed

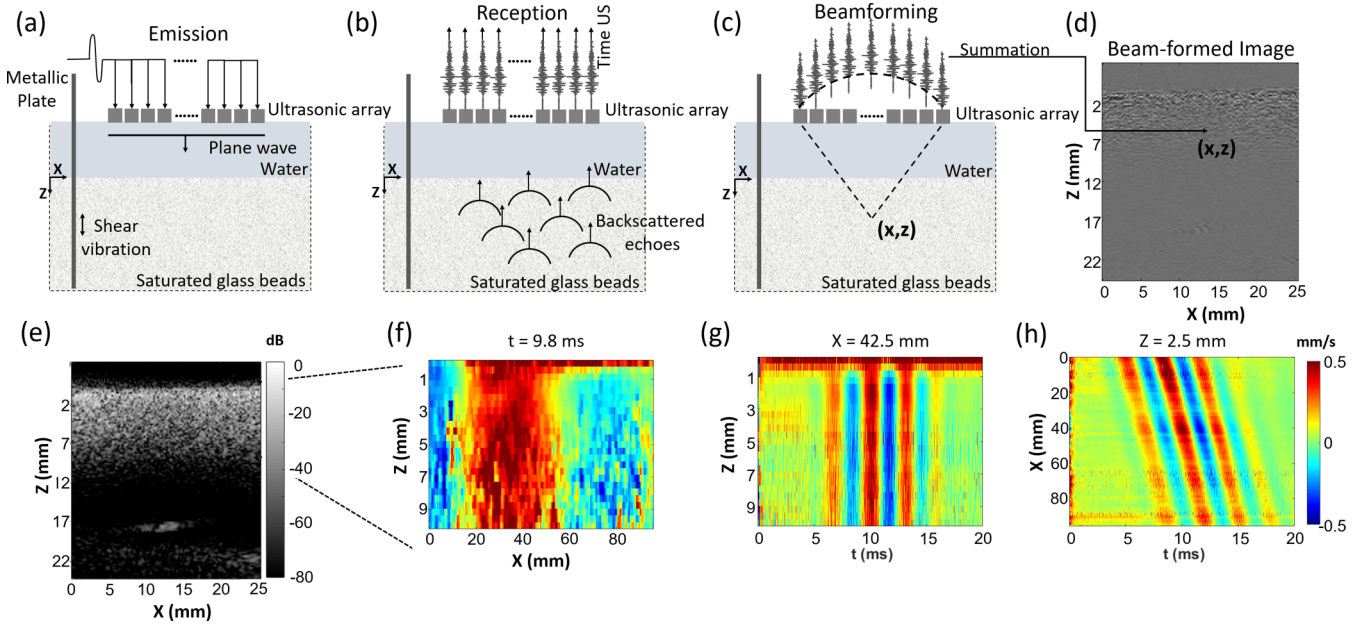


FIG. 5. (a) Ultrasound emission step: all elements in the array emit simultaneously a short pulse centered at 4 MHz, thus generating a pulsed plane wave. (b) Ultrasound reception step: the backscattered echoes coming from different locations within the medium are recorded by each element of the transducer array. (c) Beam-forming step: to relate the arrival time of an ultrasound echo to a given position within the imaging plane, each point  $(x, z)$  in the image is obtained by adding coherently the backscattered signals originating from it. (e) Logarithmic compression of the beam-formed image to increase the image contrast. A steel plate immersed in the granular medium appears as a strong echo at  $z \approx 17$  mm and  $x \approx 12$  mm. (f) One snapshot of the axial particle velocity field associated with the Rayleigh-like wave propagation at  $t = 9.8$  ms after the generation of the wave. (g) Particle velocity as a function of the depth and time at  $x = 42.5$  mm. (h) Axial particle velocity field as a function of time along  $x$  at the surface of the sample.

backscattered signals are summed. Finally, these two steps are repeated for all points within the imaging plane to generate a beam-formed image such as the one shown in Fig. 5(d).

This beam-formed image is a cross-sectional image of the sample. With the application of a logarithmic compression to increase the contrast, a steel plate immersed in the granular medium appears as a strong echo at  $z \approx 17$  mm and  $x \approx 12$  mm [Fig. 5(e)], which shows that ultrasonic backscattering is still dominated by single scattering. That is, the arrival time of the speckle signal corresponds to a specific location of the scatterers in space. Comparison between such images recorded before, during, and after the shear wave passage was used in this work to study grain rearrangement under a high shear driving amplitude [see Figs. 3(a) and 3(b)].

The axial particle velocity field  $v_z(x, z, t)$  ( $=v_{ac}$ ) associated with guided wave propagation at a given instant  $t$  after the source excitation can be obtained (at least for the first  $\sim 10$  mm of depth) by correlating in time the speckle pattern observed

from one image  $S_t(x, z)$  to the next  $S_{t+\delta t}(x, z)$  (i.e., by speckle interferometry) [32], with  $\delta t \sim 1/f_{RF}$  and  $f_{RF} = 16$  kHz the frame rate. In practice, the operation is performed after quadrature demodulation of the RF backscattered signals. The field of the axial particle velocity  $v_z$  at a particular time corresponding to the  $n^e$  frame is then inferred from [46]

$$v_z(x, z, n) = \frac{f_{RF}}{2} \frac{c}{\omega} \operatorname{atan} \left( \frac{Q(n)I(n+1) - Q(n+1)I(n)}{I(n)I(n+1) + Q(n+1)Q(n)} \right), \quad (\text{A1})$$

with  $\omega$  the central frequency of ultrasound and  $I$  and  $Q$  the in-phase and quadrature-phase components of the demodulated signal corresponding to pixel  $(x, z)$  in the image. As an example, a snapshot of the axial particle velocity field is presented at  $t = 9.8$  ms in Fig. 5(f). The map of the particle velocity as a function of the time at  $x = 42.5$  mm shows the

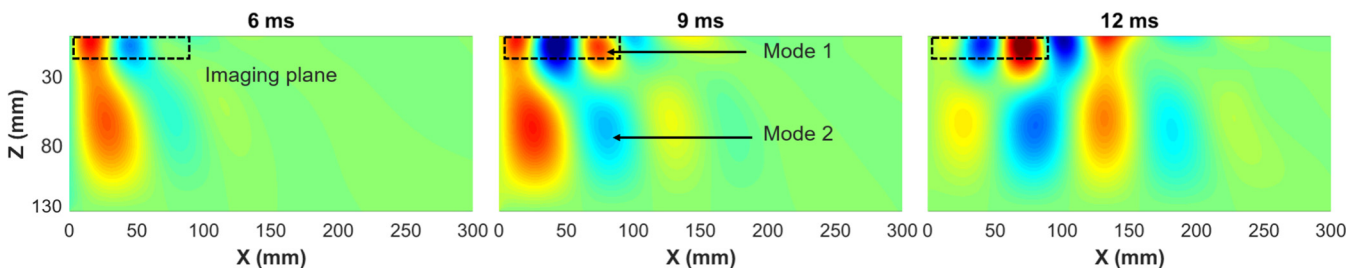


FIG. 6. Three snapshots of the vertical component of the simulated particle velocity field during wave propagation for a 300-Hz excitation. The dashed black rectangle corresponds to the imaging plane used in the experiments presented in Figs. 5(f)–5(h).

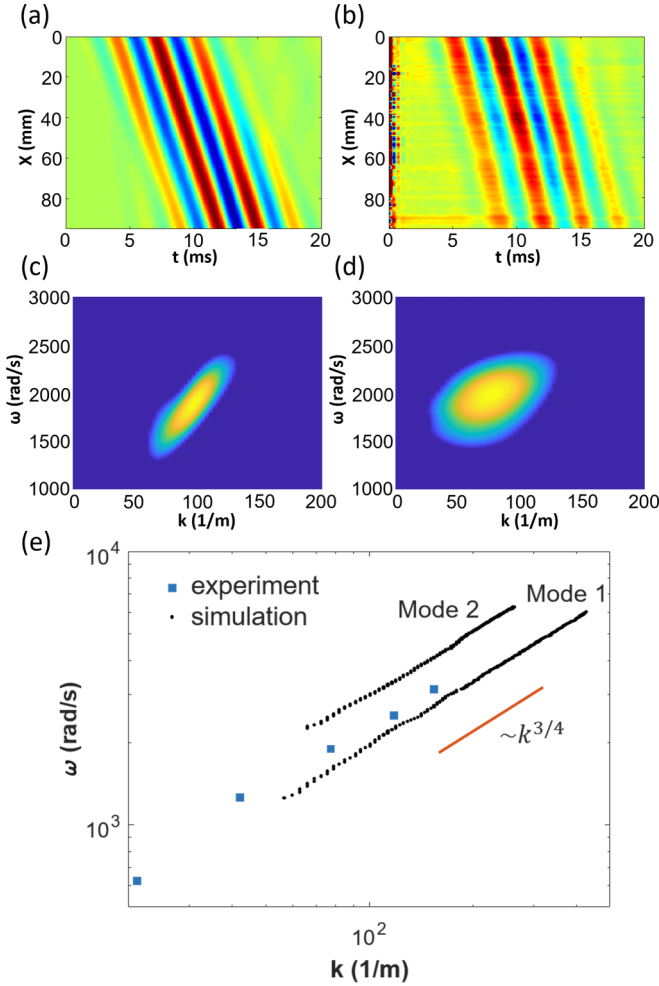


FIG. 7. Particle velocity field for a four-cycle tone burst excitation centered at 300 Hz in (a) a simulation and (b) an experiment along with its double Fourier transform in (c) and (d), respectively. (e)  $\omega$ - $k$  relation extracted from experiment (blue squares) and simulation (black dots). The relation  $\omega \propto k^{3/4}$  is plotted by the solid red line for reference.

ability to follow the wave propagation in depth [Fig. 5(g)]. Finally, Figs. 5(h) and 1(c) map the pulsed particle velocity as a function of  $x$  and time  $t$  at the surface of the sample.

## APPENDIX B: GUIDED ACOUSTIC MODES

Bonneau *et al.* [11] and Jacob *et al.* [30] have demonstrated that wave propagation along the free surface of a granular packing may be described by a superposition of localized acoustic modes. To define which guided acoustic modes are

generated with our setup [Fig. 1(a)] we conducted a series of numerical finite-element-method (FEM) simulations with COMSOL Multiphysics, following an approach similar to that proposed by Bergamo *et al.* [47]. We model the granular packing in the long-wavelength limit ( $\lambda_{LF} \gg d$ ) as a continuous elastic layer of thickness  $h = 130$  mm. A gravity-induced stiffness gradient was included in the FEM simulations given by the scaling law  $V_{P,S} = \gamma_{P,S}(\rho gz)^{\alpha_{P,S}}$ , where  $V_{P,S}$  is the compressional/shear wave velocity,  $\gamma_{P,S}$  is a depth-independent coefficient,  $\alpha_{P,S}$  is the power-law exponent,  $\rho$  is the bulk density of the medium,  $g$  is the gravity acceleration, and  $z$  is the depth. For the simulations we used  $\rho = 1700$  kg/m<sup>3</sup>,  $\alpha_S = 1/4$ , and  $\alpha_L = 1/6$  as in Refs. [8,19]. Finally,  $\gamma_S$  and  $\gamma_L$  were chosen equal to 5.25 and 14.8, respectively, as reported in Refs. [30,48] as the best-fit parameters for a dry granular packing. The boundary conditions were set as free at the surface and clamped at the bottom. Experimentally, waves are generated using a rough metallic plate acting all across the layer sample [Fig. 1(a)]. Therefore, in the FEM simulations a prescribed displacement was assigned to the plane  $x = 0$  with the same temporal dependence used in the experiments: a four-cycle tone burst centered at a frequency between 100 and 500 Hz.

Figure 6 shows three snapshots of the vertical component of the simulated particle velocity field in the  $xz$  plane for a 300-Hz excitation. Two modes of propagation are generated with our setup: a first mode localized near the free surface and a second mode that propagates within the bulk of the sample (modes 1 and 2, respectively, in Fig. 6). Due to the size of the imaging plane used in the experiments, the particle velocity is presumably dominated by mode 1 as can be verified in Fig. 7, which shows experimental and simulated particle velocity fields. Experiment and simulation are found to be in good agreement. Furthermore, the presence of a single mode of propagation may be observed in the corresponding double Fourier transformation [Figs. 7(c) and 7(d)].

The dispersion relation [depicted on a log-scale in Fig. 7(e) for both simulation and experiment] helps us to understand the nature of this mode. With simulation it was also possible to calculate the  $\omega$ - $k$  relation within the bulk of the sample at  $z = 80$  mm (mode 2 in Fig. 6). From this figure it is possible to establish that  $\omega$  reasonably follows a relation proportional to  $k^{3/4}$  (an exponent of 0.79 was found by fitting the experimental data in Fig. 7). Therefore, the mode detected by our setup corresponds to the lowest surface mode described in [30]. This type of localized surface mode is controlled by the shear wave speed profile and is reminiscent of a Rayleigh wave in an elastic homogeneous layer (i.e., without a velocity gradient). Consequently, its propagation velocity is directly linked to the shear modulus of the sample.

- [1] A. J. Liu and S. R. Nagel, *Nature* **396**, 21 (1998).
- [2] M. Cates, J. Wittmer, J.-P. Bouchaud, and P. Claudin, *Phys. Rev. Lett.* **81**, 1841 (1998).
- [3] C. S. O'Hern, L. E. Silbert, A. J. Liu, and S. R. Nagel, *Phys. Rev. E* **68**, 011306 (2003).
- [4] M. van Hecke, *J. Phys.: Condens. Matter* **22**, 033101 (2009).

- [5] D. Bi, J. Zhang, B. Chakraborty, and R. P. Behringer, *Nature* **480**, 355 (2011).
- [6] E. Brown and H. M. Jaeger, *Rep. Prog. Phys.* **77**, 046602 (2014).
- [7] E. Lerner, E. DeGiuli, G. Düring, and M. Wyart, *Soft Matter* **10**, 5085 (2014).

- [8] H. A. Makse, N. Gland, D. L. Johnson, and L. Schwartz, *Phys. Rev. E* **70**, 061302 (2004).
- [9] M. Wýart, L. E. Silbert, S. R. Nagel, and T. A. Witten, *Phys. Rev. E* **72**, 051306 (2005).
- [10] H. Mizuno, S. Mossa, and J.-L. Barrat, *Proc. Natl. Acad. Sci. USA* **111**, 11949 (2014).
- [11] L. Bonneau, B. Andreotti, and E. Clément, *Phys. Rev. Lett.* **101**, 118001 (2008).
- [12] C. F. Schreck, T. Bertrand, C. S. O'Hern, and M. Shattuck, *Phys. Rev. Lett.* **107**, 078301 (2011).
- [13] C. P. Goodrich, A. J. Liu, and S. R. Nagel, *Phys. Rev. E* **90**, 022201 (2014).
- [14] B. Andreotti, Y. Forterre, and O. Pouliquen, *Granular Media: Between Fluid and Solid* (Cambridge University Press, Cambridge, UK, 2013).
- [15] M. Otsuki and H. Hayakawa, *Phys. Rev. E* **90**, 042202 (2014).
- [16] J. Boschan, D. Vågberg, E. Somfai, and B. P. Tighe, *Soft Matter* **12**, 5450 (2016).
- [17] J. Paredes, M. A. Michels, and D. Bonn, *Phys. Rev. Lett.* **111**, 015701 (2013).
- [18] X. Jia, C. Caroli, and B. Velicky, *Phys. Rev. Lett.* **82**, 1863 (1999).
- [19] J. Goddard, *Proc. R. Soc. London A* **430**, 105 (1990).
- [20] Y. Khidas and X. Jia, *Phys. Rev. E* **85**, 051302 (2012).
- [21] M. W. Knuth, H. J. Tobin, and C. Marone, *Granular Matter* **15**, 499 (2013).
- [22] P. A. Johnson and X. Jia, *Nature* **437**, 871 (2005).
- [23] X. Jia, T. Brunet, and J. Laurent, *Phys. Rev. E* **84**, 020301(R) (2011).
- [24] S. van den Wildenberg, M. van Hecke, and X. Jia, *Europhys. Lett.* **101**, 14004 (2013).
- [25] L. R. Gómez, A. M. Turner, M. van Hecke, and V. Vitelli, *Phys. Rev. Lett.* **108**, 058001 (2012).
- [26] S. Ulrich, N. Upadhyaya, B. van Opheusden, and V. Vitelli, *Proc. Natl. Acad. Sci. USA* **110**, 20929 (2013).
- [27] V. F. Nesterenko, in *Dynamics of Heterogeneous Materials* (Springer, Berlin, 2001), pp. 307–384.
- [28] E. Han, I. R. Peters, and H. M. Jaeger, *Nat. Commun.* **7**, 12243 (2016).
- [29] I. Buttinoni, J. Cha, W.-H. Lin, S. Job, C. Daraio, and L. Isa, *Proc. Natl. Acad. Sci. USA* **114**, 12150 (2017).
- [30] X. Jacob, V. Aleshin, V. Tournat, P. Leclaire, W. Lauriks, and V. Gusev, *Phys. Rev. Lett.* **100**, 158003 (2008).
- [31] S. Catheline, J.-L. Gennisson, M. Tanter, and M. Fink, *Phys. Rev. Lett.* **91**, 164301 (2003).
- [32] B. Saint-Michel, H. Bodiguel, S. Meeker, and S. Manneville, *Phys. Rev. Appl.* **8**, 014023 (2017).
- [33] S. van den Wildenberg, X. Jia, J. Léopoldès, and A. Tourin, *Sci. Rep.* **9**, 5460 (2019).
- [34] C. Cassar, M. Nicolas, and O. Pouliquen, *Phys. Fluids* **17**, 103301 (2005).
- [35] G. Metcalfe, S. Tennakoon, L. Kondic, D. Schaeffer, and R. Behringer, *Phys. Rev. E* **65**, 031302 (2002).
- [36] D. L. Johnson and T. J. Plona, *J. Acoust. Soc. Am.* **72**, 556 (1982).
- [37] T. Bourbié, O. Coussy, and B. Zinszner, *Acoustics of Porous Media* (Editions Technip, Paris, 1987).
- [38] T. Brunet, X. Jia, and P. Mills, *Phys. Rev. Lett.* **101**, 138001 (2008).
- [39] L. Bureau, C. Caroli, and T. Baumberger, *Proc. R. Soc. A* **459**, 2787 (2003).
- [40] K. W. Winkler, *Geophys. Res. Lett.* **10**, 1073 (1983).
- [41] E. Del Gado, *Physics* **11**, 88 (2018).
- [42] J. Léopoldès, G. Conrad, and X. Jia, *Phys. Rev. Lett.* **110**, 248301 (2013).
- [43] H. Hentschel, S. Karmakar, E. Lerner, and I. Procaccia, *Phys. Rev. E* **83**, 061101 (2011).
- [44] L. Lemrich, J. Carmeliet, P. A. Johnson, R. Guyer, and X. Jia, *Phys. Rev. E* **96**, 062901 (2017).
- [45] H. Melosh, *Nature* **379**, 601 (1996).
- [46] T. Loupas, J. Powers, and R. W. Gill, *IEEE Trans. Ultrason. Ferroelectr. Freq. Control* **42**, 672 (1995).
- [47] P. Bergamo, L. Bodet, L. V. Socco, R. Mourgues, and V. Tournat, *Geophys. J. Int.* **197**, 233 (2014).
- [48] V. Gusev, V. Aleshin, and V. Tournat, *Phys. Rev. Lett.* **96**, 214301 (2006).